AIMS Materials Science, 11(4): 620–633.
DOI: 10.3934/matersci.2024032
Received: 23 May 2024
Revised: 01 July 2024
Accepted: 11 July 2024
Published: 22 July 2024

http://www.aimspress.com/journal/Materials

Research article

Holographic method for stress distribution analysis in photoelastic materials

Sidney L. da Silva[1,*], Felipe M. Prado[2], Isis V. Brito[3], Diogo Soga[3], Lígia F. Gomes[3], Niklaus U. Wetter[2] and Mikiya Muramatsu[3]

[1] Optics and Applications Group, Fatec Itaquera, 08295005, São Paulo, SP, Brazil
[2] Energy and Nuclear Research Institute, IPEN-CNEN/SP, 05508-000, São Paulo, Brazil
[3] Institute of Physics, University of Sao Paulo, 05508-090, São Paulo, SP, Brazil

*** Correspondence**: Email: sidney.silva6@fatec.sp.gov.br; grupoopticaaplicacoes@gmail.com; Tel: +55-11-999409109.

Abstract: An alternative method to obtain the internal stress distribution in photoelastic materials using digital holography (DH) is presented. Two orthogonally polarized holograms were used to obtain the phase maps and analyzed using the proposed approach. This method directly determines the stress distributions from the phase differences obtained in the reconstructed phase maps, unlike methods obtained by photoelasticity. Optical information, such as index of refraction, phase differences, etc., are not measured directly in traditional photoelasticity. However, this approach was validated with both the finite element method and the RGB (red, green, and blue) photoelasticity method that is traditionally used.

Keywords: polarized digital holography; photoelastic materials; stress and strain; polarization; RGB method; finite element method

1. Introduction

Transparent photoelastic materials represent an exciting alternative to the experimental study of stress and strain distributions induced in solids by carges. When subjected to carges, these materials present the double refraction phenomenon, or birefringence, changing the polarization state of the

transmitted light through the solids, which can be used to analyze the stress distribution [1]. The effect of double refraction, first described by Bartholinus [2–4] and related with the stress state by Brewster in the early 19th century [5], advanced throughout the 20th century with a non-destructive set of techniques and methods which associates the study of material stresses with optics, the photoelasticity [6–8]. Since the pioneering work of Coker and Filon [9–11], photoelasticity became a fundamental base for determining stress and strain distributions in photoelastic materials. Thus, great interest was generated in several fields, such as Engineering and Odontology [12–14], which validated and contributed to developing the theoretical method of finite elements [15,16].

Despite advances, most studies are qualitative or indirectly quantitative [13,14] due to the difficulties in obtaining direct optical information. Improvements in qualitative data and quantitative analysis methods are needed so that non-destructive, fast, and reliable optical methods become a reference for determining stress distribution in materials. Although holographic techniques have advanced significantly in recent years, the various works have invested very little in the stresses distribution analysis in photoelasticity using holography. The dynamics of holography allow the results to be more precise, as they are based on optical properties such as intensity, phase, refractive index, etc., which are provided directly or almost directly, thus offering a great perspective in the more quantitative treatment of problems involving elasticity mechanics [17].

We present an alternative approach to determine the stress distribution profile through a non-destructive procedure based on digital holography (DH) [18,19], allowing us to obtain quantitative intensity and phase information from light transmitted through a photoelastic material. The DH produces remarkably accurate results when combined with appropriate statistical processing of optical data, facilitating the quantitative treatment of the specific problem as outlined in the proposed methods [20]. An off-axis holographic setup was used to obtain two cross-holograms with two orthogonally polarized reference waves and a birefringent system with photoelastic samples under static loads [21–25]. After digitally reconstructed with DH, the received data generates the phase differences used to calculate the distributions of elastic stresses. The validation of the method was carried out with the methods finite elements and RGB (red, green, and blue) photoelasticity [14,16,26,27].

2. Materials and methods

2.1. Samples and Techniques

Four standard rectangular blocks, composed of mixtures of epoxy resin solutions, were prepared according to the traditional procedures [28] of the photoelastic technique, constituting the samples used in this work. The preparation of the samples involved two stages: making the silicone molds, from curing in a liquid solution and catalyst, and the photoelastic samples, from curing, in silicone molds, a liquid solution of epoxy resin and hardener. Details are presented in the work [17]. For the determinations of the mechanical and holographic parameters, two samples with different thicknesses were made, one more flexible and one less flexible. Two other samples with different thicknesses, one more and one less flexible, were also made to determine the stress distributions. Details of the procedures are presented in [17]. The more or less flexible samples were intended to help verify the order of magnitude of the stress-optical coefficient (C) and to provide a greater range of comparison with the photoelastic methodology.

The utilized holographic technique is shown in Figure 1.

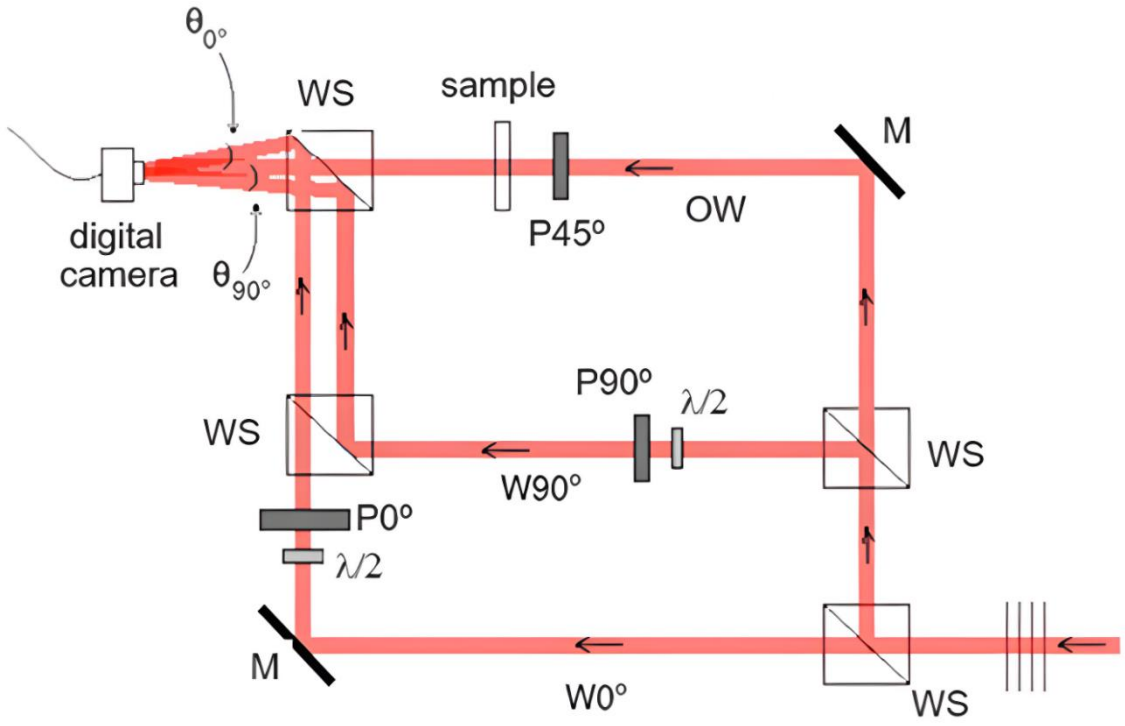

Figure 1. The holographic system measures the phase differences between the orthogonal components of the light transmitted in a birefringent system. OW: object wave; W0º: reference wave with horizontal polarization at 0º; W90º: reference wave with vertical polarization at 90º. P are polarizers. WS the wave splitters; λ/2 are half-wave plates, and M are mirrors.

A laser light source (1) was used to generate three independent waves: one object wave (OW), with the direction of polarization at 45º concerning two orthogonal reference waves, one with the direction of polarization at 0º (W0º), and another with the direction of polarization at 90º (W90º). Two distinct holograms were produced from the resulting interference patterns among OW, W0º, and W90º, propagating with different angles to the digital camera, as shown in Figure 1: θ(0º) between the OW and W0º, and θ (90º) between OW and W90º, as limited by the N-quest Theorem [29–31]. Two sets of holograms were recorded from each sample for compression and decompression in the birefringent system. The compression occurs by the progressive addition of load on the samples, and the decompression occurs by progressive removal of these loads.

The photoelastic images were obtained by blocking both reference waves, removing the wave splitter (WS), near the digital camera, and exchanging the polarizer, P45º, of the object wave for two polarizers with orthogonal polarizations, one before and another after the photoelastic sample. Figure 2 presents an experimental configuration scheme used in photoelasticity.

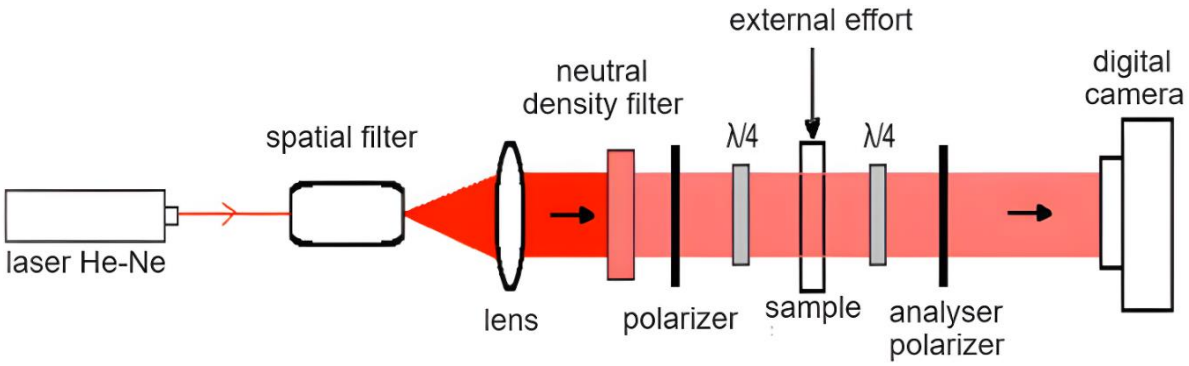

Figure 2. Schematic of the transmission brightfield elliptical polariscope. Light source with reduced intensity encounters a polarizer and a quarter-wave sheet λ/4, before interacting with the sample. It then passes through another quarter-wave blade and another analyzing polarizer. The quarter-wave blades were positioned to eliminate isoclinic fringes, which are not important for this study. Between the wave blades, a load device allows carges to be applied to the sample, changing the polarization state. The result for the observer, int the digital camera, is a pattern of isochromatic fringes.

2.2. Methods

2.2.1 Stress-optic law

The optical information obtained through photoelasticity is related to the difference between the stresses considered in the components longitudinal ($\sigma_{\parallel}$) and transverse ($\sigma_{\perp}$) to the applied load, defined by Eq 1, as given by the stress-optic law [6,17,28]:

$$n_{\parallel} - n_{\perp} = C(\sigma_{\parallel} - \sigma_{\perp}) \tag{1}$$

where C is the stress-optical coefficient, and $(n_{\parallel} - n_{\perp})$ is the difference between the refraction indexes in the components longitudinal ($n_{\parallel}$) and transverse ($n_{\perp}$) to the effort. For a material with thickness e, the refractive index difference is also associated with the phase difference $\Delta\phi$, so Eq 1 can be rewritten as Eq 2:

$$(\sigma_{\parallel} - \sigma_{\perp}) = \frac{f_{\sigma} N}{e} \tag{2}$$

where $N = \frac{\Delta\phi}{2\pi}$ is defined as the relative retardation, $f_{\sigma} = \frac{\lambda}{C}$ is the fringe value that indicates the degree of rigidity of the material, and λ is the wavelength of the light source. Using the matrix of stress-strain $(\sigma - \varepsilon)$ of the material in the stress state plane [26], the difference between the stresses in the orthogonal components, defined by Eq 3, is [17]:

$$\begin{bmatrix}\sigma_{\perp}\\ \sigma_{\parallel}\end{bmatrix} = \frac{E}{1-\nu^2}\begin{bmatrix}1 & \nu\\ \nu & 1\end{bmatrix}\begin{bmatrix}\varepsilon_{\perp}\\ \varepsilon_{\parallel}\end{bmatrix} \Rightarrow (\sigma_{\parallel} - \sigma_{\perp}) = \frac{E}{1+\nu}(\varepsilon_{\parallel} - \varepsilon_{\perp}) \tag{3}$$

E is the mechanical elasticity modulus, and ν is the Poisson's coefficient. Therefore, comparing Eqs 2 and 3, with $N = (\mathcal{E}_{\parallel} - \mathcal{E}_{\perp})$, the material fringes value can be determined by their intrinsic properties through Eq 4 [17]:

$$f_{\sigma} = \frac{eE}{1+\nu} = \frac{\lambda}{C(\lambda)} \tag{4}$$

2.2.2. Holographic analogy

The holographic method was empirically inferred and correlated with the stress-optic law. The stress difference $(\sigma_{\parallel} - \sigma_{\perp})$ occurs in the plane normal to the passage of light [26]. Due to angular displacements, the shear stresses were not considered to limit the boundary conditions and obtain the desired equation. In analogy with photoelasticity, the stress-strain matrix for the holographic parameters is given by Eq 5 [17]:

$$\begin{bmatrix}\sigma_{\perp}\\ \sigma_{\parallel}\end{bmatrix} = \frac{\mathfrak{E}}{a(1-\nu^2)}\begin{bmatrix}1 & \nu\\ \nu & 1\end{bmatrix}\begin{bmatrix}a\,\mathcal{E}_{\mathcal{H}\perp}\\ a\,\mathcal{E}_{\mathcal{H}\parallel}\end{bmatrix} \Rightarrow (\sigma_{\parallel} - \sigma_{\perp})_{holographic} = \frac{\mathfrak{E}}{(1+\nu)}\aleph \tag{5}$$

considering, by Eq 6, that

$$\mathfrak{E} = aE \tag{6}$$

$\mathfrak{E}$ is defined as the holographic elasticity modulus, and a is a dimensionless constant that relates the holography elasticity with the mechanical elasticity. $\mathcal{E}_H = \frac{1}{a}\mathcal{E}$ is defined as the relative holographic deformation and $\aleph = \frac{(\phi_{\parallel} - \phi_{\perp})_{holographic}}{2\pi} = (\mathcal{E}_{H\parallel} - \mathcal{E}_{H\perp})$ as the relative holographic retardation. Thus, the holographic dispersion can be written as the Eq 7 [17]:

$$H(\lambda) \equiv \frac{\lambda}{f_{\sigma}} = \frac{a(1+\nu)}{e\mathfrak{E}}\lambda \tag{7}$$

where, by Eq 8,

$$\mathcal{f} = \frac{e\mathfrak{E}}{a(1+\nu)} = \frac{eE}{(1+\nu)} = f_{\sigma} \Leftrightarrow H(\lambda) = C(\lambda) \tag{8}$$

$\mathcal{f}$ and f_{σ} are the fringe values obtained in holography and photoelasticity, respectively. The photoelastic fringe value is related to the wavelength of light (λ) and the photoelastic stress-optical coefficient (C). Then, analogously to what occurs with photoelasticity, there comes the holographic dispersion term, H(λ), an intrinsic property of the material whose value depends on the light wavelength, resultant from the relation between the component differences in refractive indexes, $(n_{\parallel} - n_{\perp})_{holographic}$ and the plane stresses $(\sigma_{\parallel} - \sigma_{\perp})_{holographic}$. For a given wavelength, the stress-holographic law is given by Eq 9 [17]:

$$(n_{\parallel} - n_{\perp})_{holographic} = H(\sigma_{\parallel} - \sigma_{\perp})_{holographic} \tag{9}$$

We have experimentally confirmed these equations in [21,22].

2.2.3. Fresnel transform

The off-axis configuration separates the diffraction orders during the digital reconstruction performed with FTM's fresnel transform method [17,32,33]. The image field (ψ_{mn}) and phase (ϕ_{mn}) were calculated using Eqs 10 and 11, and the corresponding maps were reconstructed.

$$\psi_{mn} = \frac{e^{ikz} \cdot e^{\frac{ikz\lambda}{2}\left(\frac{n^2}{N^2\Delta\xi^2}+\frac{m^2}{M^2\Delta\eta^2}\right)}}{iz\lambda} \cdot F\left[\Delta k_\xi, \Delta k_\eta\right] \tag{10}$$

$$\phi_{mn} = \text{arctg}\left\{\frac{Im[\psi_{mn}]}{Re[\psi_{mn}]}\right\} \tag{11}$$

where $F\left[\Delta k_\xi, \Delta k_\eta\right] = F\left[I_H(\xi,\eta) \cdot \psi_R(\xi,\eta) \cdot e^{\frac{\pi i}{z\lambda}[(n\cdot\Delta\xi)^2+(m\cdot\Delta\eta)^2]}\right]$ is the Fourier Transform of the discretized field, $\Delta k_\xi = -\frac{k\lambda}{N\Delta\xi}, \Delta k_\eta = -\frac{k\lambda}{M\Delta\eta}, \Delta\xi = \frac{z\lambda}{N\Delta h}, \Delta\eta = \frac{z\lambda}{M\Delta v}, \Delta h$ and Δv are the horizontal and vertical pixel dimensions, respectively. All the phase maps were demodulated with the Volkov Method [34].

The calibration of the setup followed the work of Colomb et al. [24] and was carried out using a quarter-wave plate as a sample. Two-phase maps reconstructed by FTM, one for each polarization, were subtracted to obtain the maps of phase differences in the function of the angle of orientation of the quarter-wave plate. The general expression for the phase difference ($\Delta\varphi$) as a function of the orientation of the quarter-wave, by Eq 12:

$$\Delta\phi = \arctan\left[\frac{\sin(2\delta)}{\cos^2(2\delta)}\right] \tag{12}$$

The process to obtain the demodulated phase maps for compression and decompression. The area selected (the rectangle on the hologram) of the hologram was processed with the FTM to obtain the frequency spectrum [17]. The chosen area (the rectangle on the frequency spectrum) of the frequency spectrum was obtained from the modulated phase map, and the Volkov method [34] was obtained from the demodulated phase map. The mean phase was determined from the phases of the pixels in the area selected from the demodulated phase map. To reduce the noise, in each phase map, a region of the phase map with no object was chosen, and the mean phase value of this region was subtracted from the phase map [17].

From the vertical phase maps of each stress applied, the load, σ_i, was calculated in the vertical holographic deformations, $\varepsilon_{H_{v-i}}$, in both processes: compression and decompression. In the same way, with the phase values of the horizontal phase maps, the horizontal holographic deformations, $\varepsilon_{H_{h-i}}$, were calculated. The mean value $\langle E \rangle$ was calculated from various values E by fitting the linear function, by Eq 13:

$$\sigma_i = \langle E \rangle \varepsilon_{H_{v-i}} \tag{13}$$

The mean value of the Poisson's coefficient, $\langle \nu \rangle$, was calculated from various values ν by fitting the linear function, by Eq 14:

$$\mathfrak{E}_{H_{h-i}} = \langle \nu \rangle \mathfrak{E}_{H_{v-i}} \tag{14}$$

In both cases, the Least Squares Method [34] was utilized.

For each horizontal line j, the phase differences, $(\phi_v - \phi_h)_j$, were obtained and, from the result, the relative retardation, $\aleph_j = (\phi_v - \phi_h)_j/2\pi$, was calculated between the dark fringes. These results, associated with the holographic parameters $\langle \mathfrak{E} \rangle$ and $\langle \nu \rangle$, allowed us to find the stress differences $(\sigma_v - \sigma_h)_{j-holographic}$ using Eq 5. The graphic $(\sigma_v - \sigma_h)_{j-holographic}$ as a function of the number of pixels produced the distributions of stress differences in the selected region.

A dimensionless constant parameter from Eq 6 gives the relation between holographic and mechanical elasticity. According to Eq 4, using the photoelastic images, mechanical parameters, $\langle E \rangle$ and $\langle \nu \rangle$, and the thicknesses, e, it is possible to calculate the photoelastic fringes, f_σ, and the photoelastic dispersions, $C(\lambda)$. Using Eq 8, the holographic parameters, E and ν, the thickness e, and the constant a, the holographic fringes, $\not{f}$, can be calculated using the phase maps. Using Eq 7 and the wavelength, λ, the holographic dispersion, $H(\lambda)$, can be calculated.

3. Results and discussion

The mechanical parameters were measured with samples sized 4.15, 2.25, and 1.03 cm, and the stress distribution was tested in samples sized 4.15, 2.25, and 4.90 cm, both in holography and photoelasticity.

Each technique was applied to only one block from each pair of standard blocks, which were prepared with identical flexibilities and labeled as –F low flexibility and +F high flexibility. Stresses were applied to the top surface of the sample blocks via a loading device, as illustrated in Figure 1.

The modified Mach-Zehnder interferometer apparatus was built with a He-Ne laser (632.8 nm CW, 20 mW, model 1135PUniphase). The photoelastic images and hologram registers were captured with a Thorlabs digital camera, model DCC1240C-HQ color, CMOS sensor, 1280 × 1024 pixels, size pixel 5.3 μm (square).

The calibration process of the holographic system generated an experimental distribution that, when compared to a theoretical curve, Figure 3, showed the reliability of the system [24].

The continuous line represents the theoretical curve, Eq 12, and the circles of the experimental distribution. The distribution of the point around the curve indicates that the adjustment of the polarization of waves is correct.

Two sets of holograms were recorded for each sample for compression and decompression. The stresses, applied to the upper central phase of the sample, ranged from 0.3 to 1.5 MPa. In holography, the mean phases were obtained from the statistics of ten selected areas in each demodulated phase map. The final mean was calculated using the values of compression and decompression.

The photoelasticity RGB method, in transmission mode, was associated with the finite elements method to determine the distributions of the stress differences in the same selected regions as those used with the holographic method. These results were used to evaluate the proposed method by comparing holography and photoelasticity by stress-optic and stress-holographic law, given by Eqs 1 and 9, respectively.

All the fitted functions used the least square method [27]. A third-degree polynomial function was fitted to the points, but all the results showed that they were linear functions.

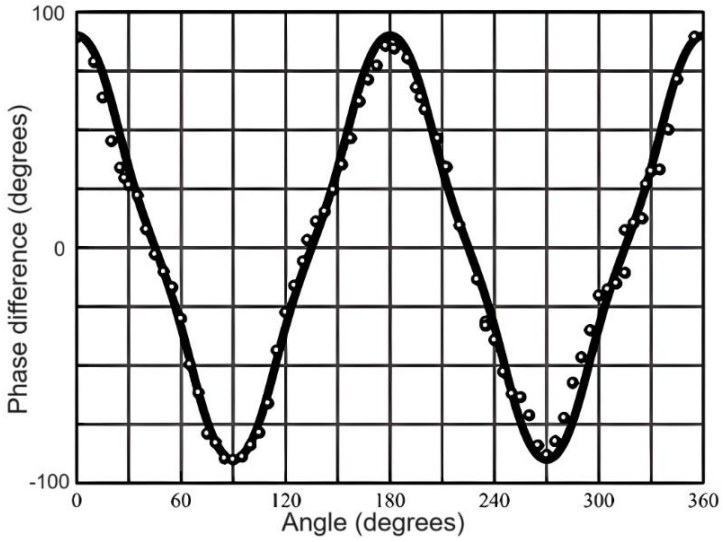

Figure 3. Graphic of the phase differences versus the angle of orientation. Theoretical curve (—) and the experimental distribution (●).

Figure 4 presents the graphics of the experimental values of the σ versus ε_v for the +F sample under compression and decompression. This graphic is used to determine the mechanical and holographic modulus of elasticity.

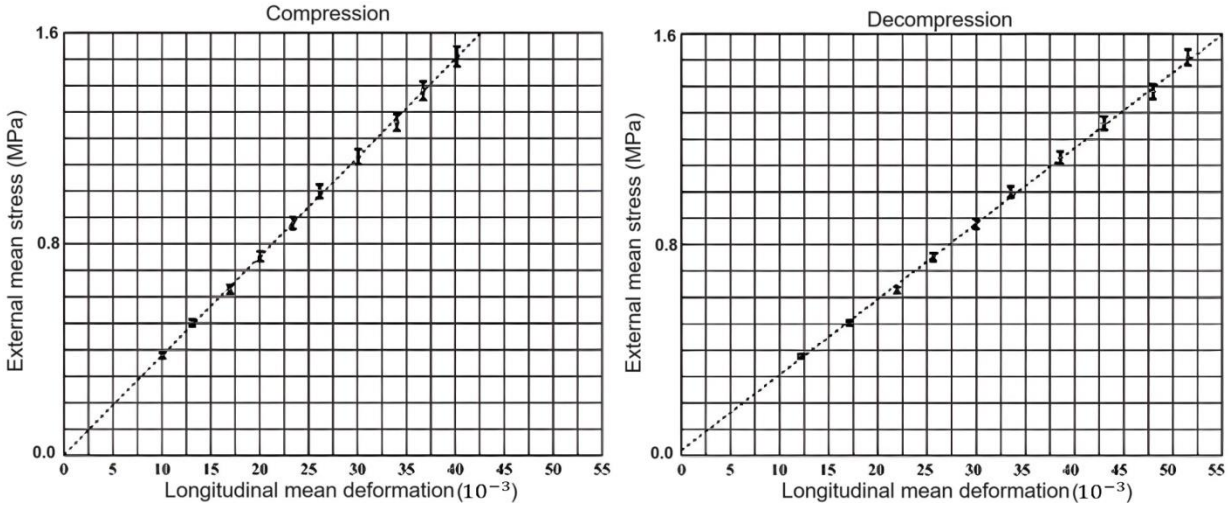

Figure 4. Graphics of external mean stress versus longitudinal mean deformation in the photoelasticity: compression and decompression.

Figure 5 presents the graphics of the experimental values of σ versus ε_{H_v} for the +F samples under compression and decompression, and they are used to obtain the Holographic and Mechanical modulus of elasticity.

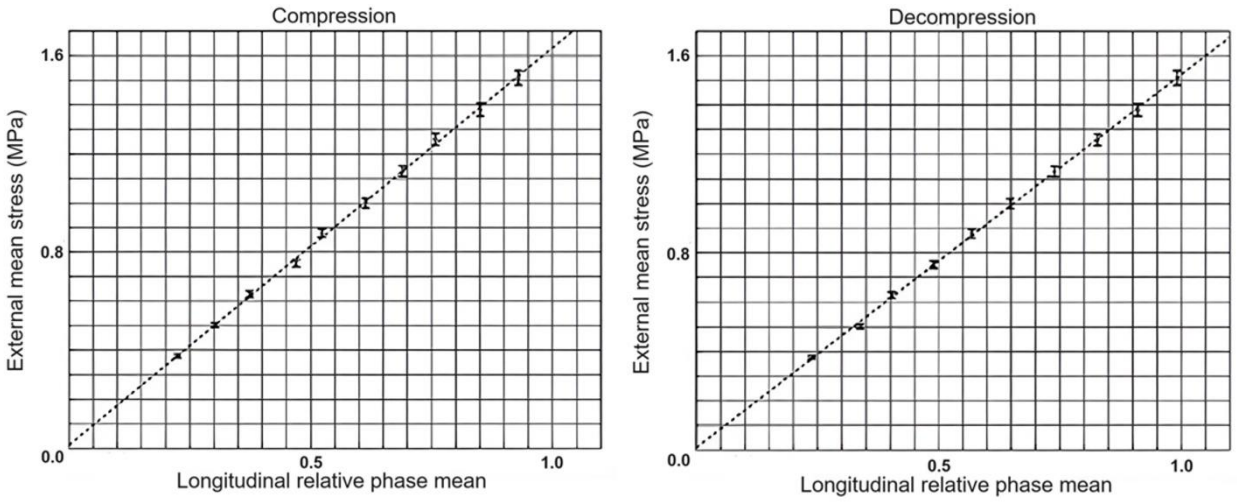

Figure 5. Graphics of external mean stress versus longitudinal relative phase mean in the holography: compression and decompression.

Similar graphs were made for the –F samples. Table 1 summarizes the holographic and mechanical modules of elasticity. The values are similar for the samples with different flexibilities in analysis. However, the rate $\mathfrak{E}/E$ differed for each method (holographic and mechanical). Considering the uncertainties, the values of $\langle \mathfrak{E}/E \rangle$ are practically equal for all samples in both flexibilities.

Table 1. Holographic and mechanical modules of elasticity in the –F and +F samples.

	–F sample (modulus of elasticity)	+F sample (modulus of elasticity)
Holography (MPa)	1.589 ± 0.032	1.320 ± 0.024
Mechanical elasticity (10 MPa)	3.35 ± 0.16	2.86 ± 0.11
$\langle a \rangle = \langle \mathfrak{E}/E \rangle (10^{-2})$	4.75 ± 0.26	4.62 ± 0.20

It was verified, in all graphics, using polynomials up to the third degree, that the best-fit function was a first-degree polynomial, related function, agreeing with Robert Hooke's theory of elasticity for the elastic regime.

Figure 6 presents the values of the $\mathcal{E}_h$ (transverse) versus $\mathcal{E}_v$ (longitudinal), used to calculate the mechanical Poisson's coefficient under the compression and decompression processes, using samples +F.

Figure 7 presents the values of the $\mathcal{E}_{H_h}$(transverse)versus $\mathcal{E}_{H_v}$(longitudinal) used to determine the holographic Poisson's coefficient under the compression and decompression processes, using samples +F to determine the stress distribution.

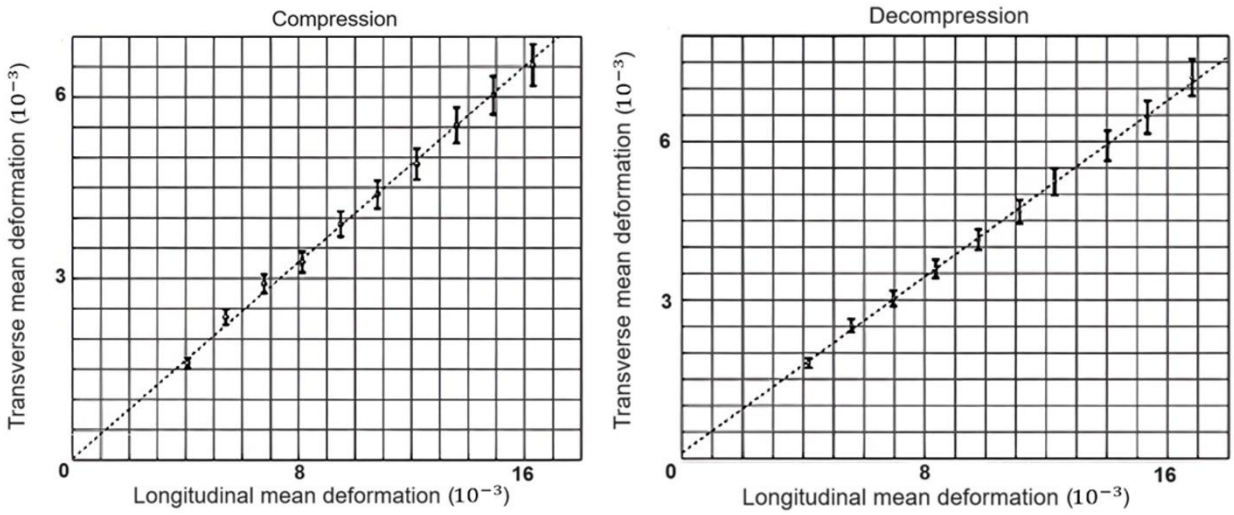

Figure 6. Graphics of transverse versus longitudinal deformation in a photoelasticity: compression and decompression.

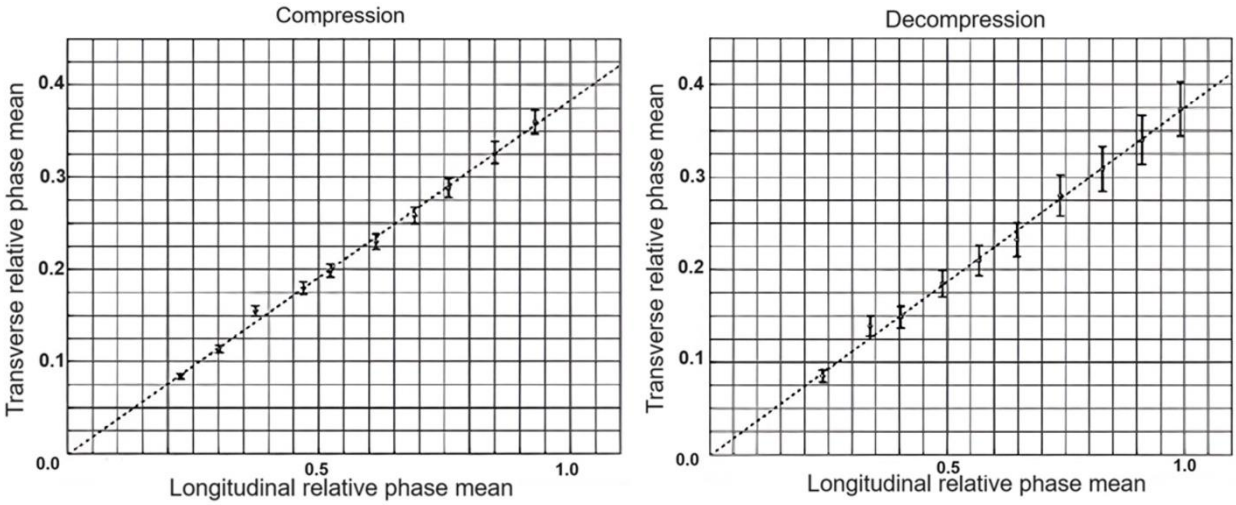

Figure 7. Graphics of transverse relative phase mean versus longitudinal relative phase mean in holography: compression and decompression.

Similar graphs were made for the –F samples. Table 2 summarizes the Poisson's coefficients: holographic and mechanical. Considering the uncertainties, the Poisson's coefficients ν are practically equal for the sample with the same flexibility.

Table 2. Holographic and mechanical Poisson's coefficients in the –F and +F samples.

	–F sample [Poisson's coefficient (10^{-1})]	+F sample [Poisson's coefficient (10^{-1})]
Holography	3.723 ± 0.022	3.735 ± 0.025
Mechanical elasticity	3.822 ± 0.095	3.90 ± 0.11

With these parameters, it was possible to determine the mean stress-optical coefficients in photoelasticity and holography, whose values are presented in Table 3.

Table 3. Holographic and photoelastic stress-optical coefficients –F and +F samples.

	–F sample [stress-optical coefficient (10^{-12} m^2/N)]	+F sample [stress-optical coefficient (10^{-12} m^2/N)]
Holography	3.921 ± 0.08	4.442 ± 0.09
Mechanical elasticity	3.95 ± 0.21	4.50 ± 0.22

The difference between the values of the samples with the same flexibility is due to the dependence of the stress-optical coefficient with sample thickness, e. However, for the same flexibility, the values agree both in holography and in photoelasticity. An important observation is that in holography, the precision of the results is better since the values are of the order of 10^{-6} N/m^2.

The graphics in Figure 8 show the distribution of stress difference over the vertical lines between two dark fringes obtained using the holographic method (●), photoelasticity RGB (+), and analytical method (▬). The load, in mass, applied was 600 g for all samples.

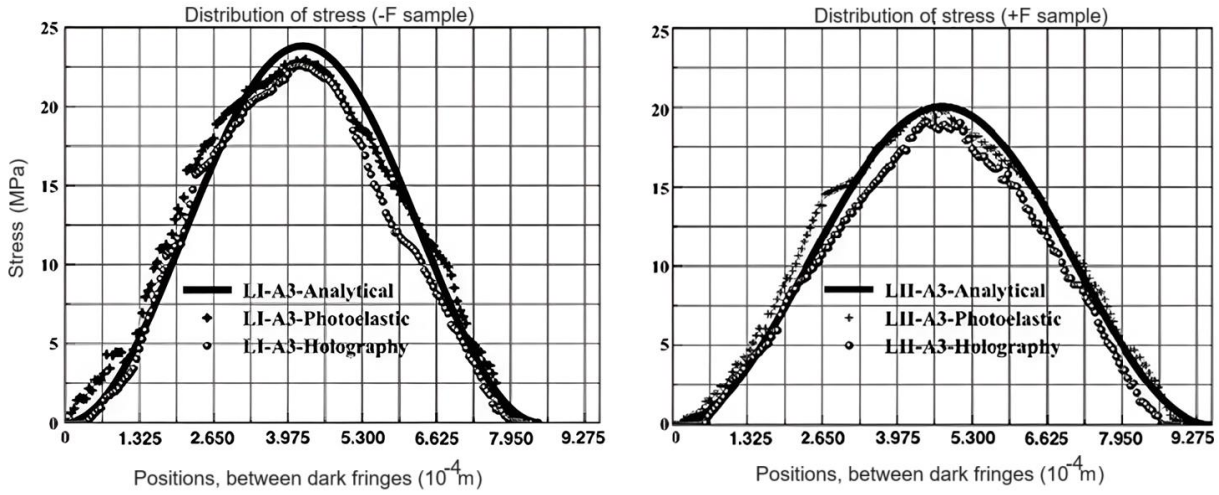

Figure 8. Graphics of the distribution of stress difference as a function of the distance between two dark fringes obtained by holography (●), photoelasticity RGB (+), and analytical (▬).

The behavior of curves in graphics exhibits similarities, indicating that the theoretical model of the proposed method is correct. The +F samples are less rigid and suffer more significant vertical deformation, reducing the modulus of elasticity under the same load. This behavior is observed graphically due to the smaller and more scattered peaks about the –F sample distribution.

In photoelasticity, the intensity of the images of the fringes pattern depends on the characteristics of the experimental configuration: transmittance of the materials, anisotropic behavior level, spectral radiation distribution of the light source (white light), the conversion factor of the light-signal control and electric-signal control, and the temporary birefringence effect. In digital holography, these effects are less relevant due to the subtractions performed in the numerical reconstruction process, which

eliminate much of this noise, and also due to the optical retardations obtained directly from the phase differences maps.

4. Conclusions

We present an alternative method to obtain the stress differences in photoelastic materials, as verified by the experiments. The similar results for the modulus of elasticity obtained through the different methods (photoelasticity, mechanical, and holographical) allowed the assumption of an analogy between Hooke's law and holography. The photoelastic and holographic dispersions are equal, allowing the establishment of the stress-holographic law in analogy with the stress-optic law. The experimental stress distributions in holography presented the same behavior as the analytic and photoelastic distributions. The results of stress distributions in holography were more accurate than in photoelasticity when compared to the theoretical results. Thus, the proposed method presents efficiency and independence in procedures since it uses only the extracted parameters obtained directly from the phase maps.

Use of AI tools declaration

The authors declare they have not used Artificial Intelligence (AI) tools in the creation of this article.

Acknowledgments

The authors are grateful for the financial support from Fundação de Amparo à Pesquisa do Estado de São Paulo (2012/18162-4, 2019/23700-4, 2022/15276-0); the physical support from Faculdade de Tecnologia de Pompeia (Fatec Pompeia), Faculdade de Tecnologia de Itaquera (Fatec Itaquera), Instituto de Física da Universidade de São Paulo (IFUSP) and Instituto de Pesquisas Energéticas e Nucleares de São Paulo (IPEN-SP).

Author contributions

The lead author (Sidney Leal da Silva) contributed theory, data, and analysis from his doctoral work [17]. The other co-authors helped with the preparation and first revisions of the article.

Conflict of interest

The authors declare no conflict of interest.

References

1. Kale S, Ramesh K (2013) Advancing front scanning approach for three-fringe photoelasticity. *Opt Laser Eng* 51: 592–599. https://doi.org/10.1016/j.optlaseng.2012.12.013
2. Moura BA (2014) Isaac Newton and the double refraction of light. *Rev Bras Ensino Fis* 36: 01–15. https://doi.org/10.1590/S1806-11172014000400021

3. Lohne JA (1977) Nova experimenta crystalli islandici disdiaclastici. *Centaurus* 21: 106–148. http://dx.doi.org/10.1111/j.1600-0498.1977.tb00350.x
4. Magie FW, Weber LR (1965) A source book in physics. *Am J Phys* 33: 247. https://doi.org/10.1119/1.1971416
5. Brewster D (1815) On the laws which regulate the polarisation of light by reflection from transparent bodies. *Philos Trans R Soc* 105: 125–159. https://doi.org/10.1098/rstl.1815.0010
6. Dally WJ (1980) An introduction to dynamic photoelasticity. *Exp Mech* 20: 409–416. https://doi.org/10.1007/BF02320881
7. Ramesh K, Kasimayan T, Simon NB (2011) Digital photoelasticity—A comprehensive review. *J Strain Anal Eng* 46: 245–266. https://doi.org/10.1177/0309324711401501
8. Ajovalasit A, Petrucci G, Scafidi M (2015) Review of RGB photoelasticity. *Opt Laser Eng* 68: 58–73. https://doi.org/10.1016/j.optlaseng.2014.12.008
9. Coker GE, Filon LNG (1932) A treatise on photo-elasticity, In: South VR, *The Mathematical Gazette*, Cambridge: Cambridge University Press, 16: 277–279. https://doi.org/10.2307/3605934
10. Frocht MM, Guernsey R (1953) A special investigation to develop a general method for three-dimensional photoelastic stress analysis. *NTRS* 2: 963–979. https://ntrs.nasa.gov/citations/19930092176
11. Föppl L, Mönch E (2013) *Praktische Spannungsoptik*, 1 Eds., Heidelberg: Springer Berlin. https://doi.org/10.1007/978-3-642-52730-2
12. Smith WC (1991) Applications of the photoelastic method to some problems in solid mechanics. *Opt Laser Eng* 14: 147–149. https://doi.org/10.1016/0143-8166(91)90045-U
13. Lee J, Yoon L, Kim YL, et al. (2016) Effect of implant number and distribution on load transfer in implant-supported partial fixed dental prostheses for the anterior maxilla: A photoelastic stress analysis study. *J Prosthet Dent* 115: 161–169. https://doi.org/10.1016/j.prosdent.2015.08.021
14. Goiato CM, Ribeiro PP, Pellizer PE, et al. (2009) Photoelastic analysis of stress distribution in different retention systems for facial prosthesis. *J Craniofac Surg* 20: 757–761. https://doi.org/10.1097/scs.0b013e3181a28a96
15. Strang G, Fix GJ (1973) An analysis of the finite element method. *Z Angew Math Mech* 55: 696–697. https://doi.org/10.1002/zamm.19750551121
16. Chen YT, Huang P, Chuang S (2014) Modeling dental composite shrinkage by digital image correlation and finite element methods. *Opt Laser Eng* 61: 23–30. https://doi.org/10.1016/j.optlaseng.2014.04.006
17. Silva SL (2016) Quantitative study of stresses in photoelastic samples using digital holography. *Institute of Physics at the University of São Paulo (IFUSP)*, São Paulo. Available from: http://www.teses.usp.br/teses/disponiveis/43/43134/tde-22102016-154751/.
18. Schnars U, Falldorf C, Watson J, et al. (2015) *Digital Holography and Wavefront Sensing*, 2 Eds., Hagen: Springer Berlin Heidelberg, 226. https://doi.org/10.1007/978-3-662-44693-5
19. Kronrod MA, Merzlyakov NS, Yaroslavskii LP (1972) Digital holography experiments. *Avtometrija* 6: 30–40. Available from: http://pascal-francis.inist.fr/vibad/index.php?action=getRecordDetail&idt=PASCAL7313011243.
20. Oliveira NG, Rodrigues CDM, Nunes SLC, et al. (2012) Digital Fourier Transform holography was applied to investigate mechanical deformation in polymers. *Opt Laser Eng* 50: 1798–1803. https://doi.org/10.1016/j.optlaseng.2012.06.016

21. Silva SL, Prado MF, Toffoli JD, et al. (2023) Characterization of the photoelastic dispersion coefficient using polarized digital holography. *J Opt Soc Am A* 40: C108. https://doi.org/10.1364/JOSAA.482543
22. Silva SL, Prado MF, Toffoli JD, et al. (2020) Measuring photoelastic dispersion coefficients in material samples with digital holography. *In Proceedings of the Practical Holography XXXIV: Displays, Materials, and Applications*. https://doi.org/10.1117/12.2544874
23. Fourney EM (1968) Application of holography to photoelasticity. *Exp Mech* 8: 33–38. https://doi.org/10.1007/BF02326248
24. Colomb T, Dahlgren P, Beghuin D, et al. (2002) Polarization imaging by use of digital holography. *Appl Optics* 41: 27–37. https://doi.org/10.1364/AO.41.000027
25. Yokota M, Terui Y, Yamaguchi I (2007) Polarization analysis with digital holography by use of polarization modulation for single reference beam. *Opt Eng* 46: 055801. https://doi.org/10.1117/1.2740601
26. Zienkiewicz OC (2005) *The Finite Element Method*, 6 Eds., London: McGraw-Hill, 1872. Available from: https://books.google.com.br/books?id=iqfue5Kv2tkC&lpg=PP1&hl=pt-BR&pg=PP1#v=onepage&q&f=false.
27. Vuolo JH (1996) *Fundamentals of Error Theory*, 2Eds., São Paulo: Blucher, 264. Available from: https://books.google.com.br/books?id=q-uyDwAAQBAJ&lpg=PP1&hl=pt-BR&pg=PP1#v=onepage&q&f=false.
28. Kuske A (1974) *Photoelastic Stress Analysis*, London: Wiley-Interscience, 519p. Available from: https://lccn.loc.gov/73002788.
29. Carcolé E, Campos J, Bosch S (1994) Diffraction theory of Fresnel lenses encoded in low-resolution devices. *Appl Optics* 33: 162–174. https://doi.org/10.1364/AO.33.000162
30. Jacquot M, Sandoz P, Tribillon G (2001) High resolution digital holography. *Opt Commun* 190: 87–94. https://doi.org/10.1016/S0030-4018(01)01046-X
31. Mann C, Yu L, Lo CM, et al. High-resolution quantitative phase-contrast microscopy by digital holography. *Opt Express* 13: 8693–8698. https://doi.org/10.1364/OPEX.13.008693
32. Schnars U, Jüptner WPO (2002) Digital recording and numerical reconstruction of holograms. *Meas Sci Technol* 13: R85. https://doi.org/10.1088/0957-0233/13/9/201
33. James DFV, Agarwal GS (1996) The generalized Fresnel transform and its application to optics. *Opt Commun* 126: 207–212. https://doi.org/10.1016/0030-4018(95)00708-3
34. Volkov VV, Zhu U (2003) Deterministic phase unwrapping in the presence of noise. *Opt Lett* 28: 2156–2158. https://doi.org/10.1364/OL.28.002156

AIMS Press

© 2024 the Author(s), licensee AIMS Press. This is an open access article distributed under the terms of the Creative Commons Attribution License (http://creativecommons.org/licenses/by/4.0)